A novel method to enhance CSL fraction, tensile properties and work hardening in complex concentrated alloys — Lattice distortion effect

Mageshwari Komarasamy[a], Shivakant Shukla[a], Nathan Ley[a], Kaimiao Liu[a], Kyu Cho[b], Brandon McWilliams[b], Raymond Brennan[b], Marcus L. Young[a], Rajiv S. Mishra[a*]

[a]Center for Friction Stir Processing, and Advanced Materials and Manufacturing Processes Institute, Department of Materials Science and Engineering, University of North Texas, Denton, TX 76203, USA

[b]Weapons and Materials Research Directorate, U.S. Army Research Laboratory, Aberdeen Proving Ground, MD 21005, USA

*Corresponding author: email ID ─ Rajiv.Mishra@unt.edu

Abstract

A framework has been developed to reduce the stacking fault energy of complex concentrated alloys (CCAs) or high entropy alloys based on increasing lattice distortion by choosing principal elements with large differences in moduli and atomic size. The framework and selection criteria have resulted in the inclusion of five CCA compositions for validation of the lattice distortion and three Fe-containing CCAs. Orientation imaging microscopy (OIM) was used to examine the fraction of special boundaries in all of the CCAs. Alloys with large lattice distortion contained high density of annealing twins. Both tensile properties and work hardening rate characteristics were evaluated. CCAs that were designed based on lattice distortion demonstrated improved ultimate tensile strength. Work hardening rate curves revealed the underlying variation in the tensile properties of various CCAs. For selected alloys, post-deformation OIM analysis of the lateral surface was carried out for establishing defect density variation.

Keywords: complex concentrated alloys; lattice distortion; tensile properties; work hardening; twinning

1. Introduction

A new class of alloy systems with multi-principle elements in equi- or non-equi-atomic compositions has been developed [1,2]. Recently, these alloys have been more broadly termed as complex concentrated alloys (CCAs), which include high entropy alloys (HEAs). Alloys with a

minimum of five elements in equimolar or non-equimolar quantities have generally been referred to as HEAs, while alloys with intermetallic phases and three principal elements are broadly referenced as CCAs [3]. The unique feature of these alloy systems is that no dominant element can be designated as the matrix element. This lack of a dominant element is a breakthrough in materials science, with the shift in compositional space from the edges or apexes of a phase diagram where one element is dominant, to the center where multiple elements are dominant. In certain compositions, mixtures of multiple principal elements have crystallized in simple face-centered cubic (FCC) [4], body-centered cubic (BCC) [4], or hexagonal close-packed (HCP) [5] crystal structures. The core effects in CCAs are the sluggish diffusion of atoms, lattice distortion, high entropy effect, and cocktail effect [6]. The presence of multiple elements of various sizes, moduli, and cohesive energy differences have been known to increase lattice distortion by shifting the elements from their FCC or BCC reference positions [7–9]. Mishra et al. [10] proposed a lattice distortion framework for designing alloys to specifically increase lattice distortion in CCAs so that fundamental deformation mechanisms could be tuned. Distortion of the lattice would have implications on the stacking fault energy (SFE), lattice friction stress, and energetics and kinetics of dislocations and twins.

SFE has been identified as a crucial parameter in the plastic deformation of conventional FCC metals and alloys, as it determines the separation distance between the two partials and, more importantly, the twinning probability. The lowest SFE values have been noted for the conventional solid solution alloy Cu-8 wt. % Al as 2.5 mJ/m^2 [11] and for the non-equiatomic CCA $Fe_{20}Cr_{26}Ni_{14}Co_{20}Mn_{20}$ as 3.5 mJ/m^2 [12]. CrCoNi [13,14], a ternary medium entropy alloy, exhibited better tensile strength, ductility, and cryogenic fracture toughness than quinary CrMnFeCoNi CCA [15]. This was attributed to twinning induced plasticity (TWIP), which was

higher in ternary CCA when compared to quinary CrMnFeCoNi CCA. In CrCoNi and CrMnFeCoNi CCAs, deformation nano-twins led to excellent cryogenic properties, second only to cryogenic steels [15]. Furthermore, in-situ transmission electron microscopy analysis revealed that nano-twins formed in front of the propagating crack, effectively bridging the propagating crack [16]. The extent of twinning or twinnability is directly correlated to SFE and both ductility and strength typically increase with the reduction in SFE. As discussed previously, alloying additions have always been key to modifying the SFE of various alloy systems. In CCAs, given the nature of the lattice, modifying the lattice distortion could also produce a reduction in SFE.

Lattice distortion in CCAs has been observed in experimental and modeling investigations [7–9,17]. As compared to FeCoCrNi and FeCoCrNiMn CCAs, Pd added FeCoCrNi CCA exhibited the largest mean lattice distortion, specifically due to large atomic size mismatch between Pd and the remaining atoms in the matrix. In these alloys, Cr-Cr and Mn-Mn atom pairs also had the largest bond distance among the remaining combinations [7]. Furthermore, pair distribution function based analysis revealed that lattice distortion of FeCoCrNiPd CCA was two times as compared to Ni80Pd20 alloy [8]. In another investigation, mean-square atomic displacements obtained from synchrotron X-ray diffraction measurements for various ternary, quaternary, and quinary CCAs correlated well with the shear modulus normalized yield strength [17]. In an investigation on Co16.67Fe36.67Ni16.67Ti30 CCA using molecular dynamics simulation, Ti atoms created large static distortions and misfit strain center, leading to large lattice distortion [9].

Overall, these investigations pinpoint two methods to increase lattice distortion in CCAs, (a) introducing relatively large atoms in the matrix of similar-sized atoms, and (b) introducing more Cr atoms that would increase lattice distortion via large bond length. In the current investigation,

both of these concepts were employed to create alloy compositions that would exhibit large lattice distortion. CrCoNi was taken as the reference alloy and alloying additions were made to modify the lattice distortion. First, the conceptual framework supporting the current investigation has been presented, and this is followed by alloy selection criteria. In total, eight CCAs were produced, and both one-step recrystallization analysis and mechanical characterization via tensile testing were carried out. A detailed work hardening mechanism study was followed by post-deformation analysis.

2. Experimental methods

$Al_{0.1}CrFeCoNi$ alloy was procured in the cast form from Sophisticated Alloys, Inc. Other seven alloys were produced from pure elements via vacuum arc melting using Al (99.9% purity), Co (99.3% purity), Fe (99.98% purity), Ni (99.95+% purity), Ti (99.99% purity) and Cr (99.3% purity) elements. During the melting process, alloys were flipped six times to ensure chemical homogeneity in a cigar-type cast. Homogenization was conducted at 1473 K for 6 hours in Ar atmosphere to further remove remnant chemical heterogeneities. After removing the thin oxide layer in the homogenized pieces, all alloys were subjected to cold-rolling reduction of ~85%. Next, one-step recrystallization was carried out at 1000ºC for 30 minutes in air followed by water quenching. By using a high annealing temperature, no secondary phases were formed in the microstructure. After recrystallization, samples were cut for electron back scattered diffraction (EBSD) analysis. Coarse polishing was performed using SiC papers, while 1 µm and 0.05 µm surface finish polishing were performed using colloidal diamond and silica suspensions, respectively. An FEI Nova NanoSEM 230 with Hikari Super EBSD system enabled orientation imaging microscopy (OIM). TSL OIM^{TM} software was used to analyze various orientation-related information. The same EBSD acquisition area of 250×250 µm^2 at a step size of 0.8 µm

was chosen for all alloys, and two scans were run per condition to confirm reliability. Tensile testing was carried out for all compositions at initial strain rate of 10^{-3} s^{-1}. Rectangular dog bone specimens with dimensions of ~5 mm gage length, ~1.23 mm width, and 1.0-1.1 mm thickness were fabricated using a CNC milling machine. All tensile samples were polished down to ~1 µm surface finish. Tensile testing was performed using a custom-built, computer-controlled tensile testing frame equipped with a 500-pound load cell. Post-deformation analysis, specifically Kernal average misorientation (KAM) analysis were carried out for $Al_{0.1}CrFeCoNi$ and $Al_{0.1}CrCoNi$ compositions. Surfaces were again polished using the same methodology described above for EBSD sample preparation. For OIM data acquisition, a fine step size of 0.3 µm was used for both scans. Fractography analysis was also carried out using a FEI Quanta 200 environmental scanning electron microscope.

3. Results and discussion

3.1 Conceptual framework

SFE is a thermodynamic quantity that denotes the ability of elements with FCC atomic stacking to exhibit an HCP stacking sequence. In pure metals, SFE is determined by bond directionality (electronic structure), and low SFE is observed in materials with less bonding directionality, for instance Cu. In alloys, solutes modify the electronic structure of the matrix element such that SFE can either be increased or decreased with alloying additions. Furthermore, solutes also tend to segregate in stacking faults, thereby stabilizing the faulted sequence, a behavior generally known as Suzuki segregation. In the case of CCAs, there is a possibility for all of these effects to occur. In addition, lattice distortion can also be significant in modifying SFE. Distorting the lattice locally always occurs in solid solution strengthening, in which a larger or smaller element (compared to the matrix) distorts the local atomic arrangements, lowering the

dislocation core energy, and eventually pinning the dislocations. In the case of CCAs, the presence of multiple elements in equi-atomic fractions distorts the lattice globally rather than just locally.

The complex interactions between multiple constituents and the consequent distortion leads to a shift in the position of atoms from their ideal FCC packing positions. In simplistic terms, the CCA lattice is distorted as compared to the ideal FCC lattice of a pure element, and the CCA exhibits a non-ideal FCC stacking. It has been well-known for decades that low SFEs result in easier formation of stacking faults and twins. In a distorted lattice, the ground state energy of an FCC crystal will be higher than the undistorted FCC lattice due to the contribution from the strain energy of distorted bonds. In this scenario, when a fault in the FCC stacking sequence is created by shuffling the atoms, the faulted HCP region will also possess non-ideal HCP stacking. Recent DFT investigations in CoCrNi CCA have observed an interesting phenomenon at 0 K in which the HCP stacking sequence exhibited low free energy when compared to FCC stacking, making HCP stacking more stable [18]. At 300 K, the contribution from lattice vibrations made FCC stacking more stable as compared to HCP stacking. Given these unique observations, the energy state of non-ideal HCP stacking of the faulted region in FCC stacking could be lower than ideal HCP stacking. Overall, the energy difference between HCP and FCC stacking ($\Delta E^{HCP-FCC}$) in the distorted condition was lower than the undistorted condition and could be given as:

$$(\Delta E^{HCP-FCC})_{Distorted} \ll (\Delta E^{HCP-FCC})_{Undistorted} \tag{1}$$

Therefore, increasing the lattice distortion would increase the energy state of FCC, thereby making a large fraction stacking faults and twins energetically favorable. This framework for reducing the SFE by increasing the lattice distortion of CCAs is shown in Figure 1. The conventional discussion on the effect of alloying additions on SFE is also presented (right side).

The correlation between lattice distortion and the natural tendency to form faults is important in designing CCAs that possess excellent twinnability and work hardenability.
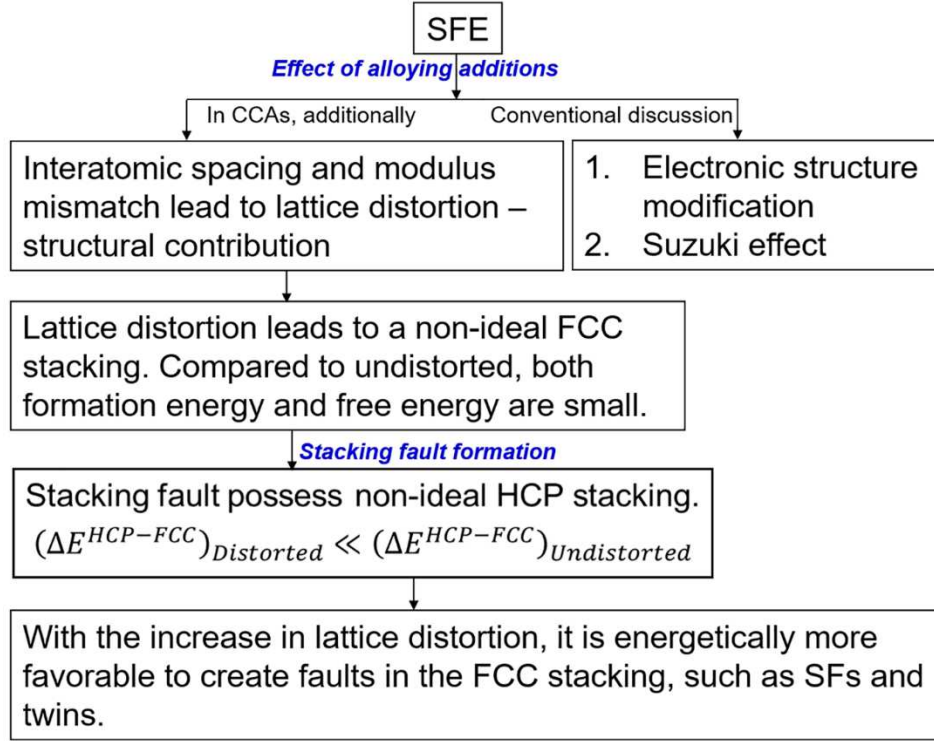

Figure 1. Overall framework for the reduction in SFE via lattice distortion core effect in the case of CCAs.

3.2 Selection criteria to increase lattice distortion

As mentioned previously, multiple formulations such as ΔS_{mix}, δ, $\Delta \chi$, and VEC have been used to differentiate the compositions that led to solid solutions and the formation of intermetallic second phases [19]. In addition to thermodynamic formulations, there are formulations that correlate lattice distortion to computable quantities. These formulations are based on inter-atomic distance mismatches whose results are similar to atomic size and bulk modulus mismatches. When combined, they can successfully predict the compositions that form solid solutions among 100+ CCA compositions [20]. While the formulation based on bulk modulus mismatch was successful in predicting phase evolution, a complete representation

requires the incorporation of two independent moduli — bulk and shear. The bond distortion in complex alloys cannot be limited to a hydrostatic compression depicted in bulk modulus values, but will also have distortion components that arise from bond shear and extension. Since all three types of bond distortion are expected to occur, the extent of the bond distortion will depend on bulk modulus (B), shear modulus (G), and Young's modulus (E) values. Table 1 gives all three moduli and B/G ratios for all elements considered. As illustrated in Table 1, Cr has the largest shear modulus and a similar bulk modulus as compared to Co, Ni, and Fe. The B/G ratios for both Co and Ni are nearly identical, while Cr falls well below them. Thus, macroscopically, as compared to Co and Ni, Cr will resist elastic shear deformation. Therefore, a large mismatch in shear modulus is expected to have implications on lattice distortion. To test this, in ternary CrCoNi CCA, the Cr fraction was increased to 1.2 and 1.3 mole fraction, and the characteristics of $Cr_{1.2}CoNi$ and $Cr_{1.3}CoNi$ CCAs were investigated and compared with CrCoNi CCA. Along with the moduli-based discussion, atomic size mismatch (δ) values for all of the alloys was calculated and has been provided in Table 1. The δ value was calculated based on the following equation [4]:

$$\delta = \sqrt{\sum_{i=1}^{n} x_i \left(1 - \frac{r_i}{\bar{r}}\right)^2}, \bar{r} = \sum_{i=1}^{n} x_i r_i \tag{2}$$

where, x_i is the atomic fraction, r is the atomic radius of elements, n is the total number of elements in a given CCA, and $\bar{r}$ is the average atomic radius. Due to larger atomic radii compared to Cr, Co, and Ni, Al and Ti atoms are expected to increase distortion of the CCA lattice. Therefore, both Al and Ti were included as minor alloying additions to CrCoNi CCA to investigate their influence on microstructure and mechanical properties. Atomic radii of the elements are presented in Table 1. As expected, δ values for Al- and Ti-containing CCAs were higher than those of the remaining alloys. Among these five alloys (CrCoNi, $Cr_{1.2}CoNi$,

$Cr_{1.3}CoNi$, $Al_{0.1}CrCoNi$, and $Ti_{0.1}CrCoNi$), the reliability of the existing δ calculation method and the importance of moduli mismatch can be investigated systematically. Furthermore, various studies have noted that Fe, despite having the same atomic size and moduli values, tends to soften the CrCoNi CCA lattice [21].So, Fe was chosen as a constituent element to soften the CCA lattice and form quaternary CrFeCoNi CCA. In addition, two well-known compositions, $Al_{0.1}CrFeCoNi$ and $Al_{0.2}CrFeCoNi$, were also selected to study the effect of Al in the Fe-containing CCAs. Values of δ for these three alloys were also calculated (based on Equation 2) and presented in Table 1. In the current investigation, distinctions were made between Fe-containing CCAs and Fe-free CCAs. To further address the difference, both $Al_{0.1}CoCrFeNi$ and $Al_{0.1}CoCrNi$ CCAs were examined. According to the atomic size-mismatch-based-lattice-distortion argument, both alloys had the same δ, and should also have similar microstructural and mechanical characteristics. However, as noted in the upcoming sections, the characteristics of these two alloys are at the opposite ends, and the negative effects of Fe on the mechanical properties are evident. In addition to moduli and atomic size difference-related analysis, $\Delta\chi$ and VEC for the alloys were also calculated [20], with values ranging from 1.8–1.82 and 8–8.25, respectively; no significant difference among the selected CCAs was noted. Furthermore, both electronic structure and bond directionality characteristics affect the way multiple principal elements stack themselves in simple FCC or BCC stacking sequence. While these hypotheses are highly theoretical and of interest for fundamental understanding, a detailed ab initio-based first-principle investigation is still necessary.

Table 1. Atomic size mismatch for various alloy systems investigated and all three moduli are also listed for all the constituent elements.

Alloys	δ	Elements	B (GPa)	G (GPa)	B/G	E (GPa)	Atomic radius, pm
CrCoNi	1.1	**Co (HCP)**	180	75	2.40	209	125

Cr$_{1.2}$CoNi	0.4	**Cr (BCC)**	160	115	1.39	279	125
Cr$_{1.3}$CoNi	0.4	**Ni (FCC)**	180	76	2.37	200	125
Al$_{0.1}$CrCoNi	2.5	**Fe (BCC)**	170	82	2.07	211	124
Ti$_{0.1}$CrCoNi	3.0	**Al (FCC)**	76	26	2.92	70	143
CrFeCoNi	0.7	**Ti (HCP)**	110	44	2.5	116	145
Al$_{0.1}$CrFeCoNi	2.3						
Al$_{0.2}$CrFeCoNi	3.1						

An overview of these eight alloys is given in Figure 2. All of these compositions were selected based on maximizing lattice distortions by increasing the difference in moduli (bulk, shear, and Young's), and the atomic size difference. All of the alloys exhibited FCC crystal structure with single-phase microstructure based on both X-ray diffraction and high magnification SEM analysis.
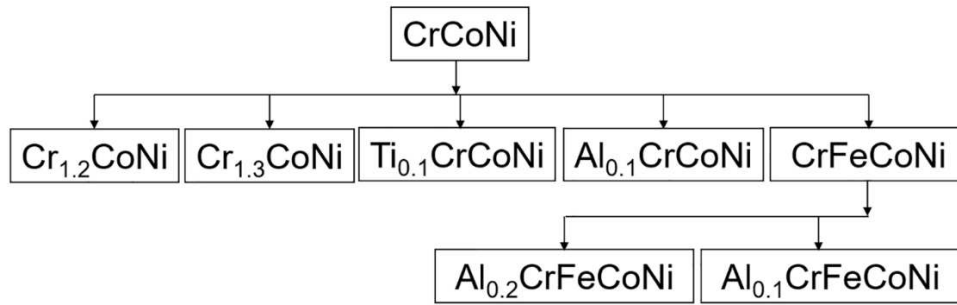

Figure 2. List of all the ternary, quaternary and quinary alloys investigated to understand the influence of lattice distortion on boundary fraction and subsequent mechanical properties.

3.3 Enhancement in the fraction of special boundaries

Inverse pole figure (IPF) maps and grain size information are shown in Figure 3 for all eight alloys. Random and special boundaries are color-coded as black and red, respectively. Note that same cold-rolling reduction (85%) and annealing procedure (30 minutes at 1000ºC) were performed for all alloys. Interestingly, Fe-containing CCAs exhibited the largest grain sizes compared to the Fe-free CCAs except for Al$_{0.1}$CoCrNi CCA. While a thorough understanding of the observation is beyond the scope of this paper, a more simplistic answer is provided. For the same rolling strain conditions, contributions from deformation twins and their consequent

dislocation storage could be different among various compositions, leading to a variation in stored energies for the material. In this case, finer grain sizes would be obtained for the materials with the highest stored energies.
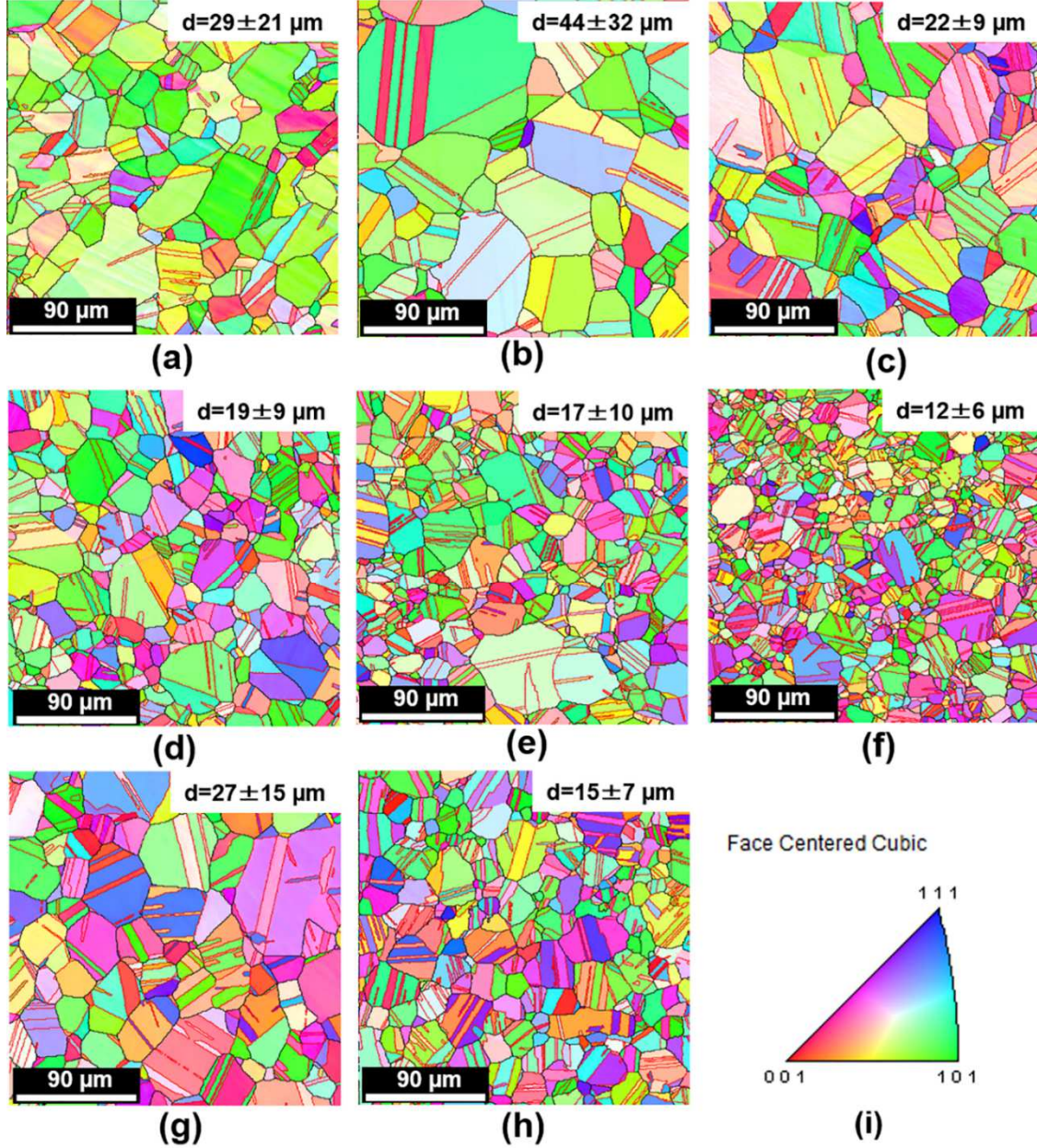

Figure 3. Grain orientation maps and grain size information of all the CCAs investigated: (a) $Al_{0.2}CrFeCoNi$, (b) $Al_{0.1}CrFeCoNi$, (c) $CrFeCoNi$, (d) $CrCoNi$, (e) $Cr_{1.2}CoNi$, (f) $Cr_{1.3}CoNi$, (g) $Al_{0.1}CrCoNi$, (h) $Ti_{0.1}CrCoNi$, and (i) [001] inverse pole figure. Special boundaries are coded in red, while random boundaries are in black.

Both the average number of twins per grain and the boundary fractions were calculated to capture the variation of microstructure in these eight alloys. The following parameters were obtained from EBSD analysis to calculate various quantities,

- L is the total length of boundaries with misorientation higher than 2° (including special boundaries),

- S is the analyzed surface area of the material,

- $L_{\Sigma 3}$ is the length of $\Sigma 3$ boundaries,

- L_{CSL} is the length of CSL boundaries,

- L_{RB} is the length of random boundaries,

- N_1 is the total number of grains excluding $\Sigma 3$ and 9 twin boundaries, and

- N_2 is the total number of grains including $\Sigma 3$ and 9 twin boundaries.

Based on these definitions obtained from [22], the computed quantities are given as follows:

1. $\Sigma 3$ fraction $= L_{\Sigma 3}/L$,

2. CSL fraction $= L_{CSL}/L$,

3. random boundary fraction $= L_{RB}/L$, and

4. average number of twin boundaries per grain $((N_2-N_1)/N_1)$.

These computed quantities are plotted in Figure 4. Boundary fraction and average number of twins per grain are shown in Figures 4 (a) and (b), respectively. In the case of Fe-free CCAs (except $Al_{0.1}CrCoNi$) in which fine grain sizes were obtained, random boundary fractions exhibited the lowest values while CSL and $\Sigma 3$ fractions were among the highest. The difference between the special and random boundary fractions was relatively large in Fe-free CCAs as opposed to Fe-containing CCAs. Another important computed quantity was the average number of twins per grain. Fe-containing CCAs exhibited a lower number of twins per grain compared to

the Fe-free CCAs. The contrast was clear when average twins per grain in $Al_{0.1}CrFeCoNi$ and $Al_{0.1}CrCoNi$ CCAs were compared. Average twin per grain values of 3.2 and 2.1 were observed in Fe-free $Al_{0.1}CrCoNi$, and Fe-containing $Al_{0.1}CrFeCoNi$ CCAs, respectively. The outlier for the Fe-free CCAs was $Cr_{1.3}CoNi$, which exhibited only marginally better values as compared to that of the CrFeCoNi CCA. This was due to the fine grain size ($\sim12\pm6$ µm) obtained for this alloy. Pande et al. [23] proposed that the grain growth accidents caused the formation of annealing twins. Therefore, the twin boundary fraction, or average number of $\Sigma3$ boundaries per grain, increased with grain size. In the current study, given the fine grain size, grain growth accidents should be limited. The same trend was observed in CoCrFeMnNi CCA, in which both twin boundary fractions and average twins per grain increased with increasing grain size, especially in the grain growth regime. On the contrary, in the recrystallization regime, no direct correlation between these quantities was observed [24]. Interestingly, both $Al_{0.1}CrFeCoNi$ and $Al_{0.2}CrFeCoNi$ CCAs exhibited the coarsest grain sizes. Based on the aforementioned model [23], $Al_{0.1}CrFeCoNi$ should have also displayed the highest number of twins per grain, which was not the case. Therefore, the presence of lattice distortions impacted the fraction of annealing twins in CCAs.
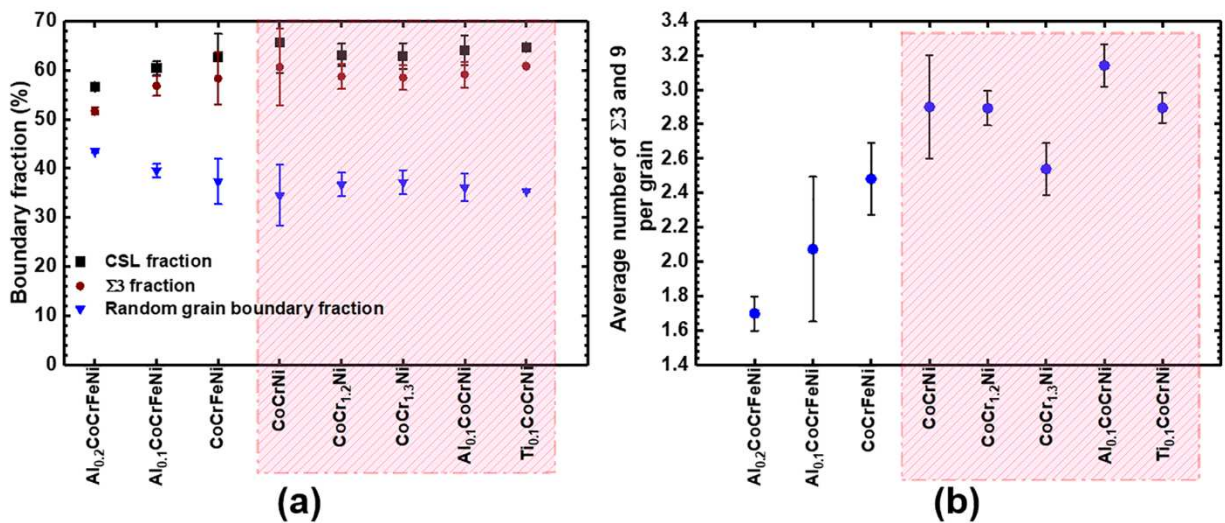
Figure 4. As a function of composition, both (a) boundary fraction, and (b) an average number of Σ3 and 9 annealing twins per grain are plotted to show the effect of lattice distortion on special boundaries. CCAs without Fe is boxed and CCAs with Fe lie outside the box.

3.4 Strength-ductility combination

Engineering stress-engineering strain and true stress-true strain curves for all compositions are shown in Figures 5 (a) and (b), respectively. Figures 5 (a) and (b) clearly reveal that the tensile properties of Fe-free CCAs are far superior to the Fe-containing CCAs. In the Fe-free CCA groups, all four alloys that were designed to increase lattice distortion displayed higher ultimate tensile strength (UTS) and yield strength (YS) when compared to the reference CrCoNi alloy. For example, with similar grain sizes, CrCoNi and $Cr_{1.2}CoNi$ showed YS values of 320±9 and 383±11 MPa, respectively. In general, the difference in YS among various single-phase CCAs is expected based on the Hall-Petch relationship,

$$\sigma_{YS} = \sigma_0 + k_{HP}d^{-1/2} \tag{3}$$

where σ_0 is the yield stress at an infinitely large grain size, d is the grain size in µm, and k_{HP} is the Hall-Petch coefficient. In the absence of precipitation strengthening, σ_0 can be equated to the combination of solid solution strengthening and lattice friction stress (σ_{PN}). Due to the complex nature of lattice distortion and its consequence on dislocation mobility, the contribution from σ_0 will be significant compared to conventional FCC metals and alloys Therefore, varying lattice distortions will inherently vary σ_0, thereby exerting influence on the overall macroscopic YS. This observation can be explained clearly by comparing the YS of $Al_{0.1}CrCoNi$ with $Al_{0.1}CrFeCoNi$ or CrFeCoNi CCAs. While variation in grain size among these three alloys was insignificant, YS varied from ~220±13 MPa in $Al_{0.2}CrFeCoNi$ or ~277 in CrFeCoNi alloys to ~340±21 MPa in $Al_{0.1}CrCoNi$ CCA.

The compilation of YS, true stress at necking, and total elongation are shown in Figure 5 (c).

14

True stress at necking varies from ~805 to ~928 MPa in Fe-containing CCAs and ~1157 to ~1494 MPa in Fe-free CCAs. Total elongation did not undergo a significant variation among the CCAs. As alluded to earlier, CrCoNi CCA was used as a reference alloy, and the remaining alloys were chosen with respect to the reference alloy based on the lattice distortion discussion. Based on the performance of various CCAs, the following observations can be made:

1. Both $Cr_{1.2}CoNi$ and $Cr_{1.3}CoNi$ alloys exhibited higher YS and UTS than CrCoNi CCA. Therefore, minor increase of an element with a large moduli (either bulk or shear) led to better tensile properties.

2. $Al_{0.1}CrCoNi$ and $Ti_{0.1}CrCoNi$ also performed better than the reference alloy CrCoNi CCA. Therefore, minor additions of either large- or small-sized atoms, as compared to the average size, can be expected to impact the lattice distortion and the resulting strength.

3. The presence of Fe suppressed the positive benefit that generally resulted in higher YS and UTS for Al- and Ti-containing CCAs, as was observed in $Al_{0.1}CrFeCoNi$ and $Al_{0.2}CrFeCoNi$.

4. True stress at necking as a function of atomic size mismatch is presented in Figure 5 (d). As observed, atomic size mismatch alone may not be a good assessment tool for producing CCAs with large lattice distortions, as $Al_{0.2}CrFeCoNi$ and $Cr_{1.3}CoNi$ exhibited the largest and smallest δ, respectively. However, the tensile deformation behavior of $Al_{0.2}CrFeCoNi$ CCA was inferior to $Cr_{1.3}CoNi$ CCA as noted from high UTS value of $Cr_{1.3}CoNi$ CCA. Moreover, the same δ values were observed for $Al_{0.1}CoCrFeNi$ and $Al_{0.1}CoCrNi$ CCAs, but tensile properties were not comparable. Zhao et al. [25] also investigated the correlation between δ and lattice friction stress. Both friction stress and

alloy strength increased with an increase in calculated δ values. However, CrCoNi alloy was not included in the comparison, which despite having a small δ exhibited high strength.

5. Fe-free CCAs demonstrated high ultimate tensile strength than Fe-containing ones, although the reason for this is not yet understood.

Work hardening rate is the net result of hardening and dynamic recovery contributions. Figure 5 (e) contains work-hardening curves for all CCAs, indicating clear changes at different stages. For clarity, only three representative conditions are shown in Figure 5 (f). Various work hardening stages, generally referenced as A, B, C and, D, are marked on the work hardening curves. The initial stage (stage A), where the work hardening rate decreases with stress or plastic strain, is known as dynamic recovery, or stage III. This stage is dominated by the dislocation recovery processes, and is temperature-, strain rate-, and SFE-dependent. One trend that is interesting to note is the slope of stage A and its variation among various CCAs, which is steepest for Fe-containing CCAs, but relatively shallow for the Fe-free CCAs. Among the CCAs, the shallowest slope was observed for $Cr_{1.2}CoNi$. Representative examples of the slopes (marked by lines) are shown in Figure 5 (f). The slope in stage III is directly correlated to defect structure evolution, such as cross-slip and dislocation annihilation. For example, materials tested at higher temperatures will exhibit steeper slopes when compared to the same materials tested at lower temperatures since increased dislocation annihilation possibilities lead to a stronger dynamic recovery contribution to the overall work hardening rate [26]. Furthermore, nanocrystalline materials are also known to exhibit steeper slopes, which is related to their inability to store dislocations, resulting in a very small contribution of hardening to the overall work hardening rate [27]. Based on this analysis, $Cr_{1.2}CoNi$ exhibited the lowest rate of dislocation annihilation

and the highest rate of hardening compared to all other CCAs. While this behavior may have been due to the lattice distortion-controlled decrease in SFE, further detailed investigation is necessary to fully understand this observation. The change in slope in the work hardening curve at the end of stage A has been uniquely correlated to the formation of deformation twins in many conventional alloys [28] and CCAs [14] that exhibit low SFE. Deformation twinning dominated regions in all three work hardening curves are marked as stages B and C (Figure 5 (f)). Though it was referred to as a twinning dominated regime, all deformation processes are expected to contribute to the overall deformation. Finally, the sudden drop in work hardening rate was also correlated to dynamic recovery, which is marked as stage D. The main point to note is the significant difference between twinning-dominated stages B and C. For instance, $Al_{0.1}CrFeCoNi$ CCA exhibited narrow B and C stages, while the $Al_{0.1}CrCoNi$ and $Cr_{1.2}CoNi$ CCAs exhibited the most extended B and C stages. Among the CCAs, $Cr_{1.2}CoNi$ displayed a shallow stage A and extended stage B that was twinning-dominated. As a result, $Cr_{1.2}CoNi$ CCA exhibited the largest total elongation, highest UTS, and highest true stress at necking. Similarly, in the case of Al-Mg-Sc alloys, a direct correlation between the slopes of stage A and uniform elongation was obtained [29]. Materials with shallow stage A slopes exhibited higher elongation values, while materials with steeper slopes resulted in rapid tensile instability and lower elongation values. Therefore, tuning the SFE via lattice distortion can be a key to create alloys with sustained work hardening stages and therefore increased overall resistance to necking and early failure.
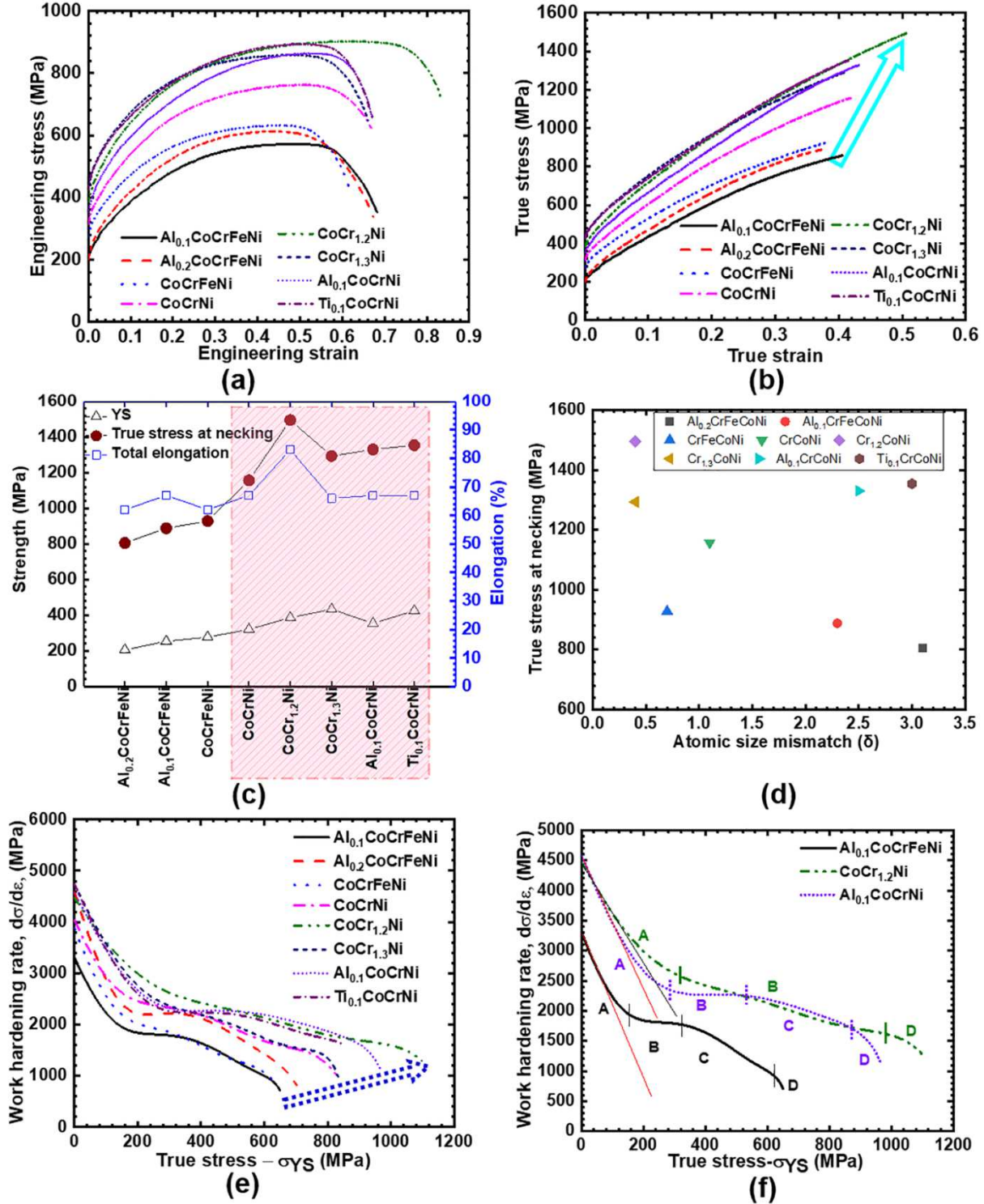
Figure 5. Engineering stress – engineering strain curves, (b) true stress – true strain, (c) summary of YS, true stress at necking, and total elongation for all the CCAs, (d) true stress at necking as a function of atomic size mismatch for all eight CCAs, (e) work hardening rate as a function of $\sigma_{flow} - \sigma_{YS}$ for all the CCAs, and (f) selected work hardening curves displaying various work hardening stages.

3.5 Post-deformation OIM analysis

OIM analysis of the failed $Al_{0.1}CrFeCoNi$ and $Al_{0.1}CrCoNi$ alloy samples after surface polishing are presented in Figures 6 (a,b) and (c,d), respectively. Figures 6 (a,c) and (b,d) represent IPF and KAM maps, respectively. In Figures 6 (a) and (c), annealing and deformation twins are marked by white and black arrows, respectively. Annealing twins were deformed, and strain accumulation in terms of KAM values were also evident. In addition to coarse annealing twins, thin and severely serrated twins were also observed, most of which originated inside the grains. These potential deformation twins have been marked with white arrows. Deformation twins in CCAs were mostly in the nanometer thickness range, and appeared to initiate and remain inside the grains. By comparing the KAM maps in Figures 6 (b) and (d), the $Al_{0.1}CrCoNi$ alloy revealed an increase in defect storage when compared to $Al_{0.1}CrFeCoNi$. For example, in the $Al_{0.1}CrCoNi$ alloy, fraction of misorientation above 0.8 was higher, and a lower fraction of the grains exhibited low misorientation regions (0-0.4º) when compared to the $Al_{0.1}CrFeCoNi$ alloy. The extent of the blue region (0-0.4º misorientation) was higher in Figure 6 (b), signifies low dislocation density. Significant defect storage was observed around both random and special boundaries, and the extent was larger in $Al_{0.1}CrCoNi$ alloys.
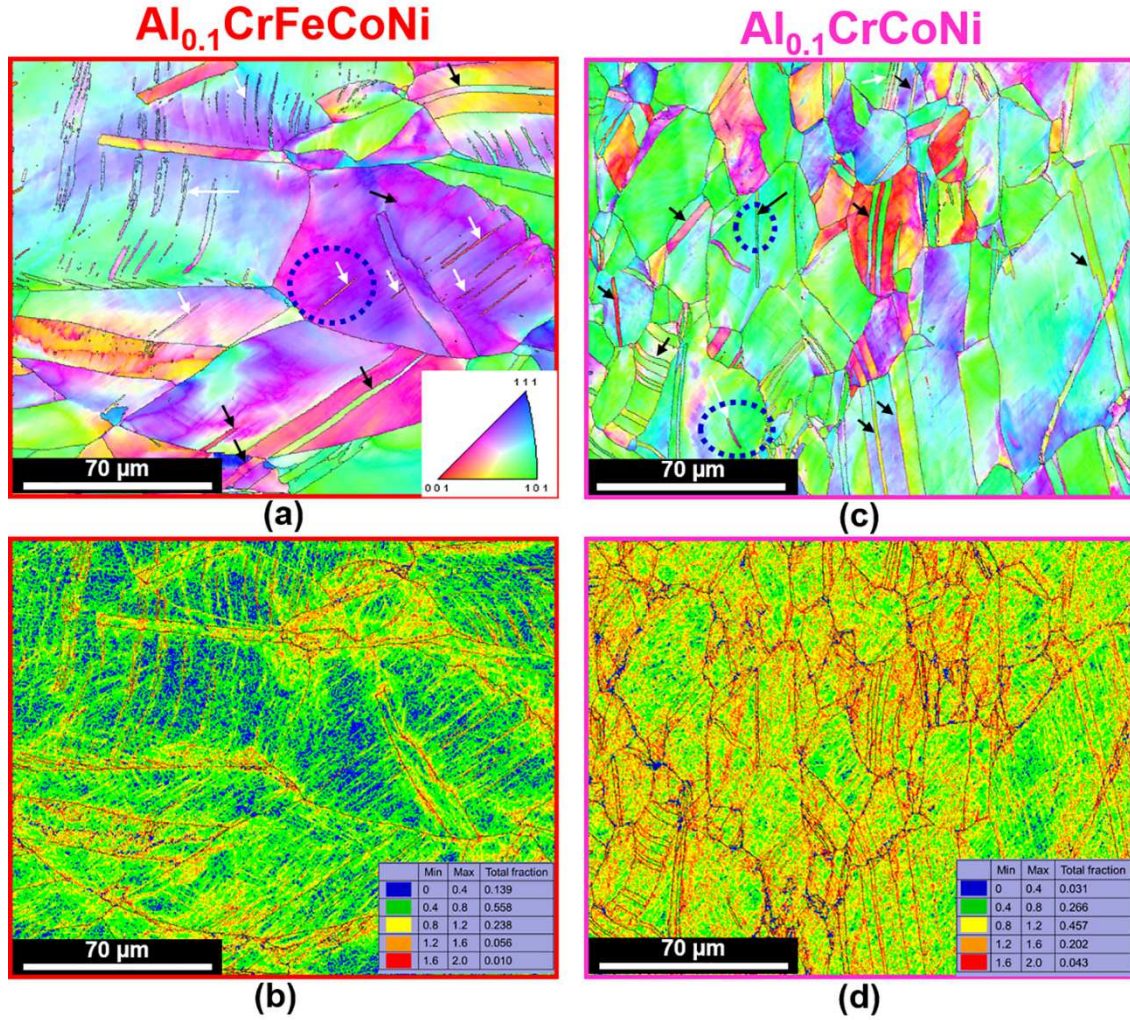
Figure 6. (a) and (b) are the IPF and KAM, respectively, for $Al_{0.1}CrFeCoNi$ alloy, and (c) and (d) are the IPF and KAM, respectively, for $Al_{0.1}CrCoNi$ alloy.

3.6 Fracture surface analysis

The fractography analyses of $Al_{0.1}CrFeCoNi$ (Figures 7 (a-c)), $Al_{0.1}CrCoNi$ (Figures 7 (d-f)) CCAs were performed in secondary electron SEM mode. The difference between Fe-containing and Fe-free CCAs was evident. In the $Al_{0.1}CrFeCoNi$ CCA, the fractional area covered by dimples was relatively small as compared to the other two CCAs. In addition, the presence of a sheared region was observed. In the dimpled regions, small and large dimple types were observed. On the other hand, in $Al_{0.1}CrCoNi$ CCA, more than ~95% of the fracture surface was covered with fine, equiaxed dimples, with the dimple ridges creating a fibrous appearance. The

20

presence of fine, shallow dimples was directly correlated to high elongation and improved work hardenability. Furthermore, very small voids were observed in both CCAs (high magnification SEM images in Figures 7 (c,f)). These voids were present either inside dimples or along the dimple walls. It was also noted in the literature that TWIP steels exhibited large fractions of micro-voids during tensile deformation as compared to Cu and Ni alloys, but the reason for this observation was not provided [30]. One explanation could be based on twinning and other associated stress concentrators. Mutual interaction of twins, twin-grain boundary interactions, and dislocation-twin interactions have been known to act as stress concentrators at intersecting interfaces. Upon critical stress concentration, nucleation of micro-cracks and voids would be highly likely. Furthermore, the density of these micro-cracks could also correlate with the fractions of various twin-related interactions. Hence, the CCAs that demonstrated very good work hardenability might also have large fractions of micro-voids.
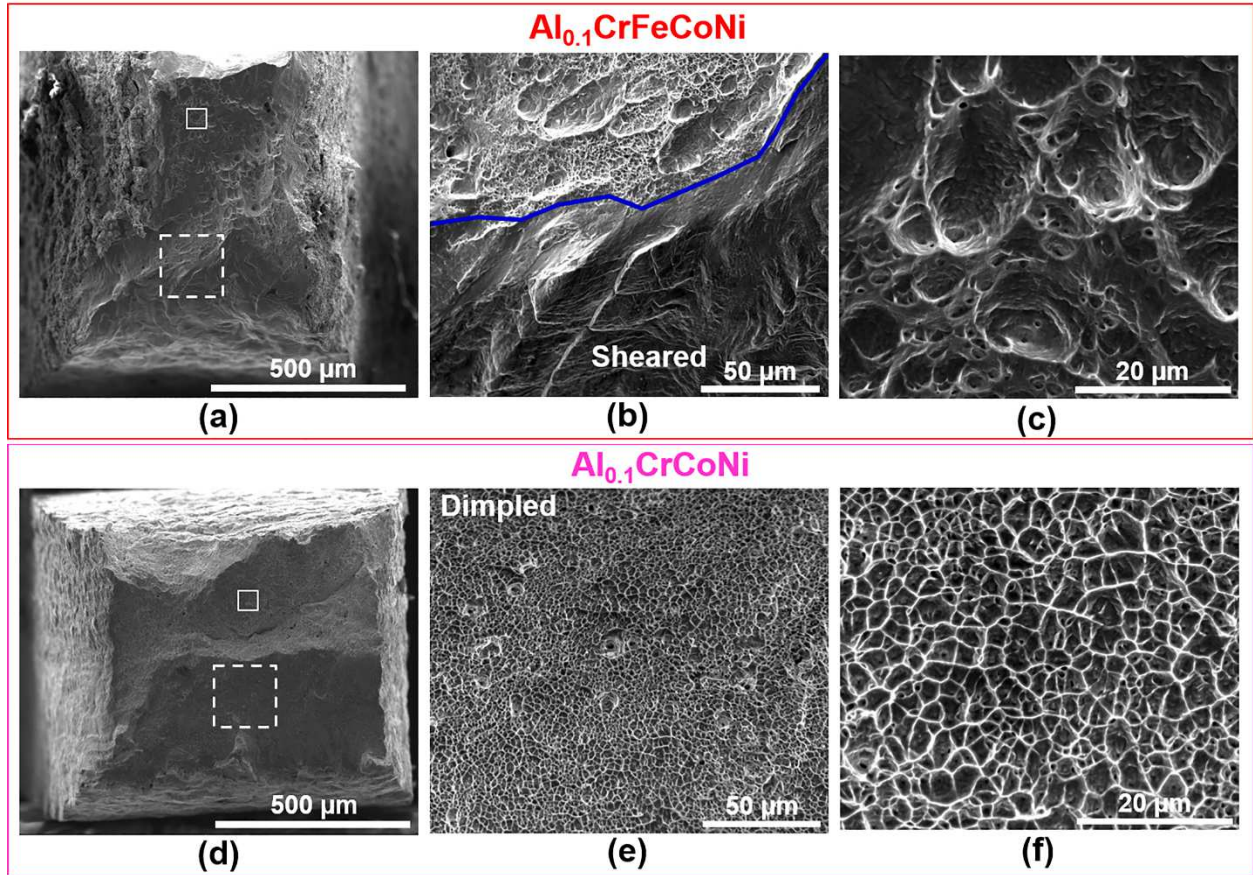
Figure 7. Fracture surfaces of (a–c) $Al_{0.1}CrFeCoNi$ and (d–f) $Al_{0.1}CrCoNi$. Distinct differences in the extent of dimpled fracture area and size of the dimples are clear. Areas marked by dashed square box in (a) and (d) are shown in (b) and (e), respectively. Areas marked by solid square box in (a) and (d) are shown in (c) and (f), respectively.

4. Conclusions

The main objective of this work was to design CCAs to understand the core effect of lattice distortion. The following conclusions are presented:

1. Larger grain size was observed in all Fe-containing CCAs, as well as the $Al_{0.1}CrCoNi$ alloy. The average number of annealing twins per grain and CSL fraction were higher in Fe-free CCAs compared to Fe-containing CCAs.

2. Tensile properties of all five Fe-free CCAs were superior to Fe-containing CCAs. In Fe-free alloys, all four alloys designed based on atomic size differences and modulus mismatches

demonstrated higher UTS than the reference alloy CrCoNi.

3. Among all the alloys, Fe-free CCAs displayed an extended twinning-dominated regime, which explained the excellent tensile properties. Furthermore, the $Cr_{1.2}CoNi$ alloy demonstrated a shallow stage III slope along with extended twinning regime.

4. Post-deformation EBSD analyses revealed that defect storage was higher in $Al_{0.1}CrCoNi$ as compared to $Al_{0.1}CrFeCoNi$, supporting the observed tensile behavior.

5. $Al_{0.1}CrCoNi$ CCA exhibited higher fractions of fine dimples when compared to $Al_{0.1}CrFeCoNi$ alloys.

Overall, the framework developed to decrease SFE based on increasing lattice distortion by choosing elements with large differences in atomic size and modulus worked out well for Fe-free CCAs. The lattice distortion-controlled SFE reduction framework can be used to effectively design new, complex concentrated alloys with increased twinnability and damage tolerance characteristics.

References

[1] J.W. Yeh, S.K. Chen, S.J. Lin, J.Y. Gan, T.S. Chin, T.T. Shun, C.H. Tsau, S.Y. Chang, Nanostructured high-entropy alloys with multiple principal elements: Novel alloy design concepts and outcomes, Adv. Eng. Mater. 6 (2004) 299–303.

[2] B. Cantor, I.T.H. Chang, P. Knight, A.J.B. Vincent, Microstructural development in equiatomic multicomponent alloys, Mater. Sci. Eng. A. 375–377 (2004) 213–218.

[3] D.B. Miracle, Critical Assessment 14: High entropy alloys and their development as structural materials, Mater. Sci. Technol. 31 (2015) 1142–1147.

[4] Y. Zhang, T.T. Zuo, Z. Tang, M.C. Gao, K.A. Dahmen, P.K. Liaw, Z.P. Lu, Microstructures and properties of high-entropy alloys, Prog. Mater. Sci. 61 (2014) 1–93.

[5] M. Feuerbacher, M. Heidelmann, C. Thomas, Hexagonal High-entropy Alloys, Mater. Res. Lett. 3 (2014) 1–6.

[6] J.W. Yeh, Alloy design strategies and future trends in high-entropy alloys, Jom. 65 (2013) 1759–1771.

[7] Y. Tong, G. Velisa, S. Zhao, W. Guo, T. Yang, K. Jin, C. Lu, H. Bei, J.Y.P. Ko, D.C. Pagan, Y. Zhang, L. Wang, F.X. Zhang, Evolution of local lattice distortion under irradiation in medium- and high-entropy alloys, Materialia. Article in Press (2018) 1–9.

[8] Y. Tong, S. Zhao, K. Jin, H. Bei, J.Y.P. Ko, Y. Zhang, F.X. Zhang, A comparison study of local lattice distortion in Ni80Pd20binary alloy and FeCoNiCrPd high-entropy alloy, Scr. Mater. 156 (2018) 14–18.

[9] S.I. Rao, C. Varvenne, C. Woodward, T.A. Parthasarathy, D. Miracle, O.N. Senkov, W.A. Curtin, Atomistic simulations of dislocations in a model BCC multicomponent concentrated solid solution alloy, Acta Mater. 125 (2017) 311–320.

[10] R.S. Mishra, N. Kumar, M. Komarasamy, Lattice strain framework for plastic deformation in complex concentrated alloys including high entropy alloys, Mater. Sci. Technol. 31 (2015) 1259–1263.

[11] O. Johari, G. Thomas, Substructures in explosively deformed Cu and Cu-Al alloys, Acta Metall. 12 (1964) 1153–1159.

[12] A.J. Zaddach, C. Niu, C.C. Koch, D.L. Irving, Mechanical properties and stacking fault energies of NiFeCrCoMn high-entropy alloy, Jom. 65 (2013) 1780–1789.

[13] B. Gludovatz, A. Hohenwarter, K.V.S. Thurston, H. Bei, Z. Wu, E.P. George, R.O. Ritchie, Exceptional damage-tolerance of a medium-entropy alloy CrCoNi at cryogenic temperatures, Nat. Commun. 7 (2016) 1–8.

[14] G. Laplanche, A. Kostka, C. Reinhart, J. Hunfeld, G. Eggeler, E.P. George, Reasons for the superior mechanical properties of medium-entropy CrCoNi compared to high-entropy CrMnFeCoNi, Acta Mater. 128 (2017) 292–303.

[15] B. Gludovatz, A. Hohenwarter, D. Catoor, E.H. Chang, E.P. George, R.O. Ritchie, A fracture-resistant high-entropy alloy for cryogenic applications, Science. 345 (2014) 1153–1158.

[16] Z. Zhang, M.M. Mao, J. Wang, B. Gludovatz, Z. Zhang, S.X. Mao, E.P. George, Q. Yu, R.O. Ritchie, Nanoscale origins of the damage tolerance of the high-entropy alloy CrMnFeCoNi, Nat. Commun. 6 (2015) 1–6.

[17] N.L. Okamoto, K. Yuge, K. Tanaka, H. Inui, E.P. George, Atomic displacement in the CrMnFeCoNi high-entropy alloy - A scaling factor to predict solid solution strengthening, AIP Adv. 6 (2016) 1-8.

[18] Z. Zhang, H. Sheng, Z. Wang, B. Gludovatz, Z. Zhang, E.P. George, Q. Yu, S.X. Mao, R.O. Ritchie, Dislocation mechanisms and 3D twin architectures generate exceptional strength-ductility-toughness combination in CrCoNi medium-entropy alloy, Nat. Commun. 8 (2017) 1–8.

[19] D.B. Miracle, O.N. Senkov, A critical review of high entropy alloys and related concepts, Acta Mater. 122 (2017) 448–511.

[20] I. Toda-Caraballo, P.E.J. Rivera-Díaz-del-Castillo, A criterion for the formation of high entropy alloys based on lattice distortion, Intermetallics. 71 (2016) 76–87.

[21] Z. Wu, H. Bei, G.M. Pharr, E.P. George, Temperature dependence of the mechanical properties of equiatomic solid solution alloys with face-centered cubic crystal structures, Acta Mater. 81 (2014) 428–441.

[22] W. Wang, F. Brisset, A.L. Helbert, D. Solas, I. Drouelle, M.H. Mathon, T. Baudin, Influence of stored energy on twin formation during primary recrystallization, Mater. Sci.

Eng. A. 589 (2014) 112–118.

[23] C.S. Pande, M. a. Imam, B.B. Rath, Study of annealing twins in fcc metals and alloys, Metall. Trans. A. 21 (1990) 2891–2896.

[24] F. Otto, N.L. Hanold, E.P. George, Microstructural evolution after thermomechanical processing in an equiatomic, single-phase CoCrFeMnNi high-entropy alloy with special focus on twin boundaries, Intermetallics. 54 (2014) 39–48.

[25] Y.Y. Zhao, T.G. Nieh, Correlation between lattice distortion and friction stress in Ni-based equiatomic alloys, Intermetallics. 86 (2017) 45–50.

[26] A.D. Rollett, U.F. Kocks, A Review of the Stages of Work Hardening, Solid State Phenom. 35–36 (1993) 1–18.

[27] H.S. Kim, Y. Estrin, Strength and strain hardening of nanocrystalline materials, Mater. Sci. Eng. A. 483–484 (2008) 127–130.

[28] S. Asgari, E. El-Danaf, S.R. Kalidindi, R.D. Doherty, Strain hardening regimes and microstructural evolution during large strain compression of low stacking fault energy fcc alloys that form deformation twins, Metall. Mater. Trans. A. 28 (1997) 1781–1795.

[29] N. Kumar, M. Komarasamy, R.S. Mishra, Plastic deformation behavior of ultrafine-grained Al-Mg-Sc alloy, J. Mater. Sci. 49 (2014) 4202–4214.

[30] C.L. Yang, Z.J. Zhang, P. Zhang, Z.F. Zhang, The premature necking of twinning-induced plasticity steels, Acta Mater. 136 (2017) 1–10.